Initial rise of bubbles in cohesive sediments by a process of viscoelastic fracture

C. K. Algar,[1] B. P. Boudreau,[2] and M. A. Barry[2]

[1] An understanding of the mechanics of bubble rise in sediments is essential because of the role of bubbles in releasing methane to the atmosphere and the formation and melting of gas hydrates. Past models to describe and predict the rise of other buoyant geological bodies through a surrounding solid (e.g., magmas and hydrofractures) appear not to be applicable to bubbles in soft sediments, and this paper presents a new model for gas bubble rise in soft, fine-grained, cohesive sediments. Bubbles in such sediments are essentially "dry" (little if any free water) and grow through a process of elastic expansion and fracture that can be described using the principles of linear elastic fracture mechanics, which assume the existence of a spectrum of flaws within the sediment fabric. By extending this theory, we predict that bubbles initially rise by preferential propagation of a fracture in a (sub) vertical direction. We present a criterion for initial bubble rise. Once rise is initiated, the speed of rise is controlled by the viscoelastic response of the sediments to stress. Using this new bubble rise model, we estimate rise velocities to be of the order of centimeters per second. We again show that capillary pressure plays no substantive role in controlling bubble growth or rise.

Citation: Algar, C. K., B. P. Boudreau, and M. A. Barry (2011), Initial rise of bubbles in cohesive sediments by a process of viscoelastic fracture, *J. Geophys. Res.*, *116*, B04207, doi:10.1029/2010JB008133.

1. Introduction

[2] Methane occurs in marine sediment owing to either methanogenesis or catagenesis. If production rates of this methane are high, the gas may saturate the pore waters and bubbles will form. Dissolution or "melting" of gas hydrates can also result in the formation of gas bubbles. A growing bubble may eventually reach a size whereby it will begin to rise through the sediments and be released into the overlying water column. The mechanics of this rise and critical size to initiate rise are currently unknown.

[3] The release of bubbles from sediments to the overlying water column has been observed in many lacustrine and marine environments [e.g., *Martens and Klump*, 1980; *Hovland and Judd*, 1988; *Chanton et al.*, 1989; *Judd*, 2003; *Ostrovsky*, 2003; *Walter et al.*, 2006, 2007a, 2007b]. Such releases, particularly from wetland sediments (marine and freshwater), constitute a significant source of atmospheric methane [*McGinnis et al.*, 2006; *Zhuang et al.*, 2009], particularly in northern latitudes.

[4] For this reason an understanding of the mechanisms behind bubble rise and migration through sediments is necessary, but little attention has so far been paid to the mechanics of this phenomenon. This dearth of knowledge is not surprising when considering the challenges of studying bubbles in sediments. Sediments are an opaque medium; it is difficult to study a bubble if you cannot see it. Therefore most evidence of gas bubbles in sediments has been obtained indirectly, either by measurements of methane concentrations or through acoustics. Such methods can provide indications of the presence of gas but say nothing about the sizes, shapes, or movements of bubbles.

[5] Recently this problem has been partially resolved through the use of computed tomography (CT) scanning technology, which has allowed the visualization of sedimentary gas bubbles [*Orsi and Anderson*, 1994; *Abegg et al.*, 1994; *Best et al.*, 2004; *Reed et al.*, 2005]. *Boudreau et al.* [2005] present a 3-D CT image of a gas bubble formed in a fine-grained sediment by gas injection. The thin "cornflake-like" shape of the bubble in the work of *Boudreau et al.* [2005] strongly suggests a fracture-based mechanism of growth. A cross section from a similar CT image is shown in Figure 1.

[6] We note, however, that such a crack-like shape is not the only gas bubble morphology observed in sediments. *Boudreau et al.* [2005] also make note of spherical bubbles in sandy sediments. Evidence of spherical bubbles in sandy sediments is also provided by *Bons and Milligen* [2001] and *Bons and Saesoo* [2003]. Such spherical bubbles clearly grow by a different mechanism (plastic or fluid deformation?).

[7] *Jain and Juanes* [2009] provide some evidence for the role of grain size in determining how gas accumulates in uncemented sediment. They developed a discrete particle model describing the invasion of a gas phase into a saturated sediment matrix. Their results indicated that grain size plays

[1]The Ecosystems Center, Marine Biological Laboratory, Woods Hole, Massachusetts, USA.
[2]Department of Oceanography, Dalhousie University, Halifax, Nova Scotia, Canada.
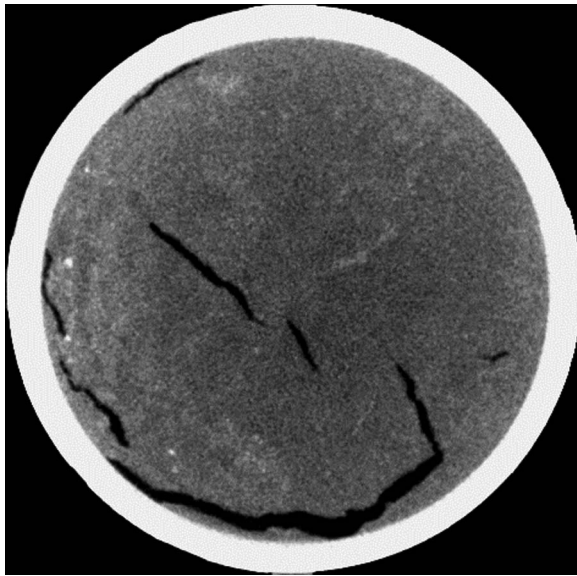
Figure 1. Cross section of a core containing gas-filled fractures (i.e., black surrounded by gray sediment) in soft muddy marine sediment collected from East Bay, Mississippi. The fractures were formed by gas injection by the methods of *Johnson et al.* [2002] and *Boudreau et al.* [2005]. The core was imaged using X-ray computed tomography.

a key role in determining the nature of this gas invasion (i.e., bubble type). In coarse-grained sediments (sands), gas percolates through the sediment framework, resulting in large regions of "dry" sediment (i.e., intergranular pore space drained of water). In fine-grained sediments, high gas-entry pressures prevent capillary invasion; instead, sediment grains are forced apart and migration results in the initiation and propagation of a (dry) fracture. These contrasting bubble shapes underlie the complexity of granular media and the variability of the stress response displayed by natural sediments.

[8] In this paper we present a theory to account for the mechanical response of cohesive, soft, clay-bearing sediments to describe bubble migration upward through cohesive sediments and to predict both the critical size to initiate rise and the speed of this rise.

2. Background Theory

2.1. Nature of Sediment Bubbles

[9] Owing to doubts and confusion expressed by the reviewers of this paper (and several others we have published), we must begin with a detailed explanation of the nature of bubble growth in soft sediments. To describe bubble growth by fracture, *Johnson et al.* [2002] put forth a theory based on the principles of linear elastic fracture mechanics (LEFM). This theory has been coupled to a methane production/transport model [*Gardiner et al.*, 2003; *Algar and Boudreau*, 2009] to predict bubble growth rates.

[10] LEFM was originally developed to characterize brittle fracture in materials such as glass and ceramics [*Broek*, 1982], and it has found use in describing rock fracture mechanics. Recently a variety of authors have, maybe somewhat surprisingly, been able to use this theory

to describe fracture in softer geological materials, such as marine muds. Figure 1 shows a cross section of a CT image of a sediment core containing a fracture formed by gas injection, in a manner similar to *Johnson et al.* [2002]. The shape of this bubble suggests a brittle fracture mechanism. *Barry et al.* [2010] present a number of images of bubbles in fine-grained (muddy) sediments formed by fracturing through gas injection and show that the geometry of these bubbles agrees with LEFM theory. Additionally, *van Kessel and van Kesteren* [2002] have carried out extensive experimental work into gas production and accumulation in soft sewage sludge, a material similar to sediment. These
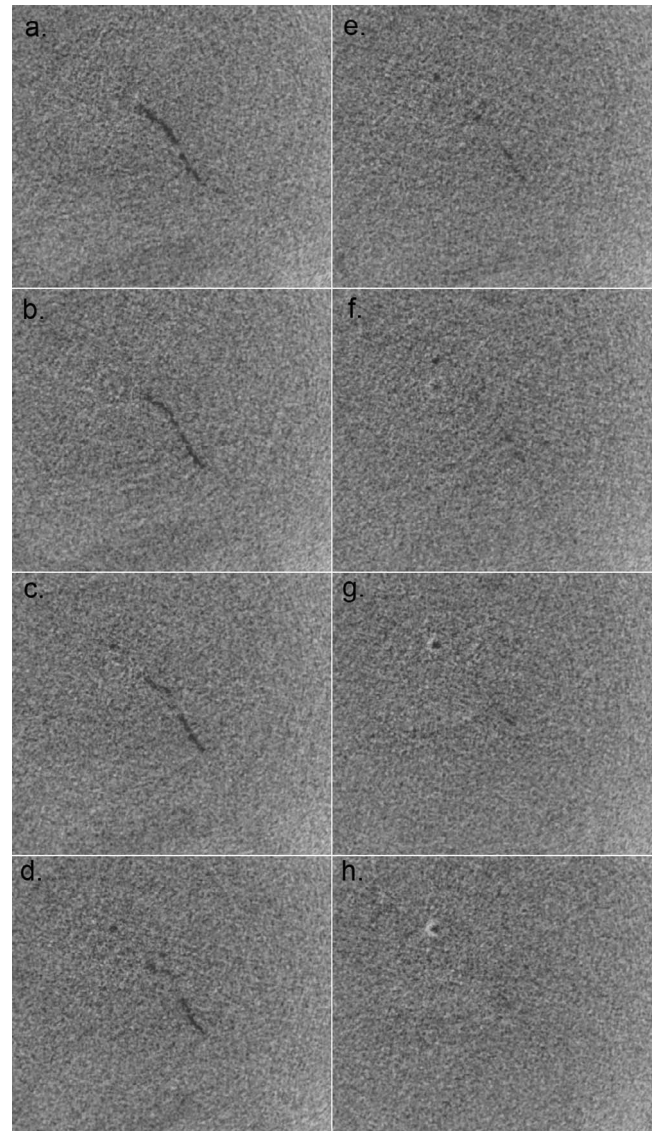

Figure 2. X-rayed cross sections of a gas bubble injected into a soft, cohesive sediment. The X-ray slices are taken at 47 μm resolution and spaced 160 μm apart (vertical). Figure 2a shows 960 μm above the bottom (tip) of the bubble, Figure 2g shows the tip, and Figure 2h shows the sediment 160 μm below the bubble. The circular object in Figures 2f and 2g is the gas injector tip. The sediment is medium gray, and the gas is black. Water, if present in the bubble, would be an intermediate gray.
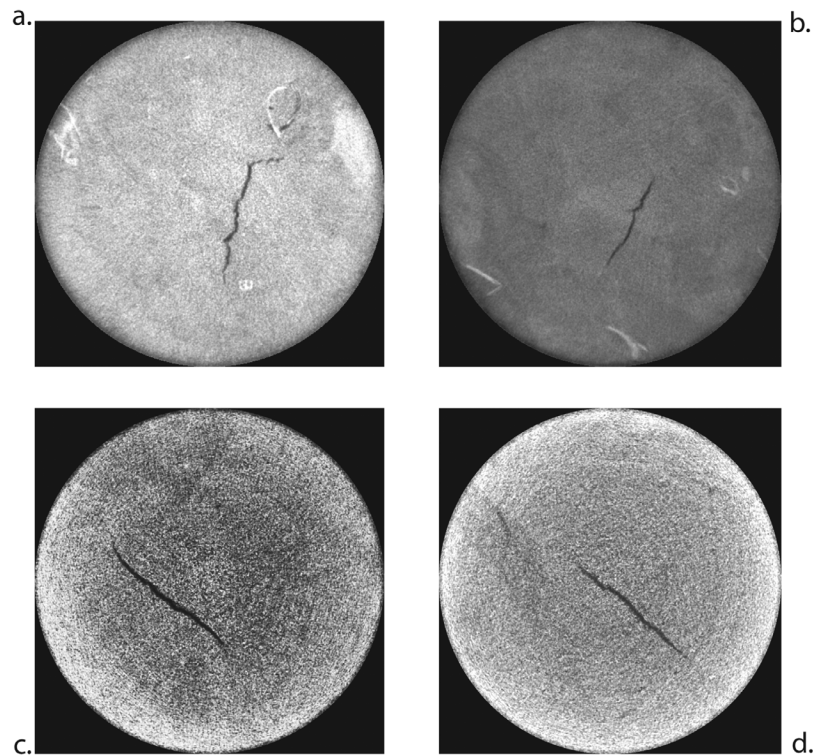
Figure 3. X-rayed cross sections of various bubbles in sediments. (a) Bubble 6-6-7-05 with 89.6 mm field of view (pixel size 175 μm). (b) Bubble 13-6-8-05 with 89.6 mm field of view (pixel size 175 μm). (c) Bubble 29-1D2-v2 with 47 mm field of view (pixel size 46 μm). (d) Bubble 29-2D2-v2 with 38 mm field of view (pixel size 37 μm).

authors made numerous observations of bubbles growing through the initiation and propagation of fractures and also found that these cracks can be described by using LEFM [*van Kessel and van Kesteren*, 2002; *Winterwerp and van Kesteren*, 2004].

[11] There is no apparent liquid water in the gas bubbles that we have studied. Figures 1–3 display X-ray cross sections of bubbles we have grown in muddy sediments. These are all taken at high resolution (i.e., 37–175 μm pixels) with over 30 K units of density discrimination (16 bit). Gas and water can easily be distinguished under these conditions.

[12] Figure 2 is a sequence of X-ray slices from 960 ìm above the bottom of a bubble (Figure 2a) to 160 μm below the bubble. Careful examination shows no water and only gas as the bottom is neared. We have similar images for a dozen bubbles and none display water at the base. These essentially "dry" bubbles are completely in accord with the previous observations from *Anderson et al.* [1998] and *Best et al.* [2004], who do not identify any water within their imaged bubbles.

[13] Figure 3 contains random horizontal slices through vertical bubbles. Again the gas is the dark (black) color of the bubbles, and there is no indication of water even as a coating along the surface and edge of the bubble. Free water would be obvious as material darker than the sediment, but lighter than the gas in the crack, and within the cracks.

[14] While growing, and rising, bubbles do take advantage of preexisting flaws in sediments, including small fractures; free water is not observed, as best as we can determine.

Most of these flaws are initially closed and partially annealed; the gas reopens them, but little water is there to be displaced. We make these points to emphasize that free water in the bubbles is certainly not essential for their dynamics and probably plays little, if any, role.

[15] A LEFM model for bubbles in soft sediment requires that this material respond to stress in a linear elastic manner. Although it is unlikely that the stress response of most sediments is truly linearly elastic, it has been shown that linear elasticity is an acceptable approximation for loadings of the magnitude experienced by the sediments during bubble growth [*Johnson et al.*, 2002]. To demonstrate this linearity, *Johnson et al.* [2002] and *Barry* [2010] performed uniaxial stress/strain measurements over the narrow range of stresses and strains observed during bubble growth. To ensure a recoverable elastic response was being measured, rather than a plastic response, all measurements of displacements were made during unloading. Figure 4 contains an example of a linear and reversible stress-strain diagram for a soft, clay-bearing, cohesive sediment. The resulting linear relationship is justification for the use of Hooke's law as a useful approximation in models for the stress/strain relationship in such sediments.

[16] In the LEFM model of bubble growth, the bubble shape is approximated by a very thin oblate spheroid, with a major axis, 2a, and minor axis, 2b; in LEFM terminology such a shape is referred to as a "penny-shaped" crack. The gas in the bubble exerts a pressure on the bubble walls, forcing the crack open and inducing stresses in the
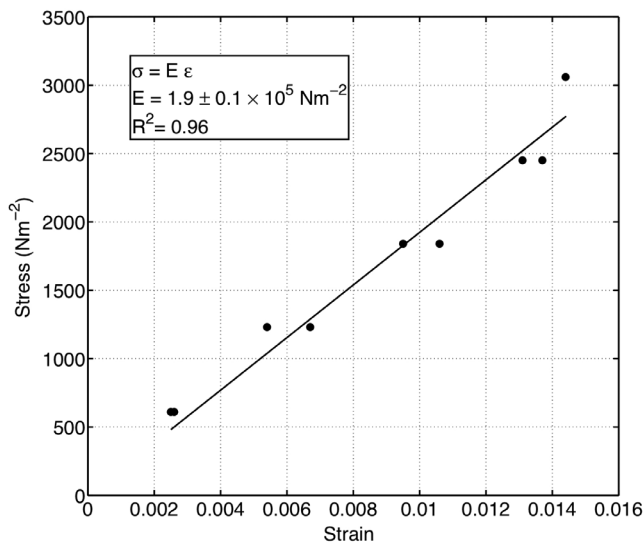
Figure 4. An example of a linear and reversible stress-strain diagram for a cohesive sediment from Nova Scotia, Canada. This is true Hookean elasticity with a Young's modulus of 1.9×10^5 Nm^{-2} [*Barry*, 2010].

surrounding sediment. This results in the concentration of tensile stresses at the crack tip. The stresses in the vicinity of the crack tip are characterized by a stress intensity factor, K_1; that is,

$$K_1 = \frac{2}{\pi} \sigma \sqrt{\pi a}, \tag{1}$$

where σ is the internal bubble pressure in excess of the ambient pressure and a is half the major axis of the spheroid, which is also referred to as the crack length. LEFM states that there is a critical stress intensity that a material can support; this is known as the fracture toughness, K_{1c}, and is a material property. If the stress intensity rises above K_{1c}, a fracture will propagate. According to LEFM, growth can occur in two ways. At low stress ($K_1 < K_{1c}$), growth occurs by elastic expansion, which expands the width of the bubble, $2b$, but not the length, $2a$. At high stresses ($K_1 > K_{1c}$) the sediment fails and the fracture is propagated; this increases the length of the bubble, decreases the width, and causes the internal bubble pressure to drop, in turn causing another phase of elastic expansion to begin. As a result, growth occurs through alternating cycles of elastic expansion and fracture.

[17] As argued by *Barry et al.* [2010], bubbles whose growth is governed by equation (1) will obey a similarity relationship that links their aspect ratio, a/b, or more conveniently, its inverse, to a dimensionless grouping of the fracture mechanical properties; that is,

$$\frac{b}{a} = \frac{4\sigma(1 - \nu^2)}{\pi E}, \tag{2}$$

where E is Young's modulus and ν is Poisson's ratio. Figure 5 is a plot of the predicted, equation (2), and observed inverse aspect ratios (IAR) of bubbles in gelatin of various strengths and those we have observed in muddy

sediments [*Barry et al.*, 2010]; the black line is a 1:1 relationship, and the data are consistent with this trend, arguing strongly for the validity of the LEFM growth model.

[18] Contrary to earlier models of bubble growth [e.g., *Wheeler*, 1988], and widely quoted in the relevant geological literature, capillarity plays no significant role in controlling the growth rate of the bubbles described above. Capillarity affects bubble stability and growth in three ways: (1) If a bubble has a wetted area, surface tension would oppose bubble expansion; (2) if surface tension at the pore mouths along the surface of a bubble is too small, the gas will escape into the pores, leading to loss of bubble cohesion; and (3) capillary pressure at the bubble tip might control the timing of bubble expansion by fracture rather than fracture toughness. We will address each of these points.

[19] *Johnson et al.* [2002, Appendix B] calculated the effect of capillary pressure from a thin coating of water along the wall of the bubble between the gas and the sediment, if present. For an oblate spheroid shape at constant volume the capillary pressure, p_c, can be estimated from

$$p_c = \gamma \left(\frac{1}{r_1} + \frac{1}{r_2} \right), \tag{3}$$

in which r_1 and r_2 are the major and minor axes and γ is the surface tension. For a typical small bubble volume of 0.015 cm^3 in our studies, we can determine r_1 and r_2 as 0.398 and 0.023 cm, respectively. The resulting capillary pressure is 0.339 kPa. This is the maximum value, which falls as the bubble grows. Typical excess (total-ambient) pressures measured by *Johnson et al.* [2002] in growing bubbles are initially of the order of 5–15 kPa; therefore
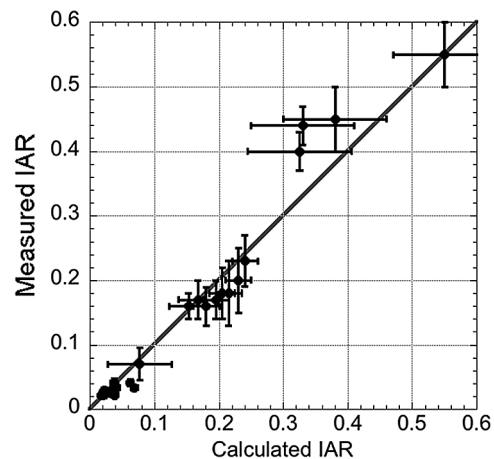

Figure 5. Plot of the measured inverse aspect ratios (IARs) and the calculated theoretical IARs for all gelatin and sediment samples in the work of *Barry et al.* [2010]. Sediment samples are the data in the lower left-hand square. Errors in calculated IARs are based on the range of measured values of Young's modulus in each sample (i.e., maximum and minimum values of E), while errors in measured IARs are taken to be 25% owing to human error in the estimation predominantly of bubble width, but also of bubble length and precision of the computed tomography scanner (sediment only).

Table 1. Capillary Pressures at Pore Throats[a]

Capillary Pressure (Pa)	Pore Throat Radius (μm)
7,400	20
14,800	10
29,600	5
49,333	3

[a]As calculated using the formula $P = 2\gamma/r$ and assuming a surface tension of 0.074 N m^{-1}.

capillary pressure can be ignored to first order as a significant impediment to bubble expansion.

[20] As to gas loss through the bubble surface, we are certain that gas does not leak out because the internal gas pressure never reaches a value high enough to overcome the capillary pressure for a pore throat. Table 1 shows the capillary pressure for a selected pore throat radius; the clay-bearing sediments we studied have pore sizes ≤20 μm and require 7–50 kPa of internal pressure to leak gas into the pores. Excess internal pressures we have measured in bubbles we have grown are of the order of 3–10 kPa, with the larger values in the finer grained sediments. (Contrast 3 kPa with 7 kPa and 10 kPa with 50 kPa to compare properly.) Thus the internal pressures are always below the capillary pressure needed to drive gas into a pore along the bubble surface. This result is consistent with the previously mentioned results of *Jain and Juanes* [2009].

[21] Finally, capillary pressure along the surface prevents gas loss, but does this capillarity pose a significant barrier at the "tip" of the bubble? *Pilkey et al.* [2008] provide a formula for the stress concentration, σ_c, at the tip for a 2-D elliptic shape; unfortunately, there is no 3-D formula, but there is no reason to believe that the result would be dissimilar. Their equation is

$$\sigma_c = p_e\left(1 + 2\frac{a}{b}\right) \qquad (4)$$

where p_e is the excess pressure in the bubble and a/b is the aspect ratio of the bubbles. We have measured the aspect ratios of bubbles in sediments, and these are of the order of 20 (see Figure 4). Using this value, we find that the stress is increased by a factor of 41 at the tip; thus, excess pressure will be of the order of 120–400 kPa, many times the capillary pressure for a pore near the tip. Capillary pressure becomes an entirely negligible issue in this case.

[22] In addition, a model of bubble growth, and rise, in cohesive, fine-grained sediments need not consider molecular level effects that may be important in rock fracture [e.g., *Bui*, 1998], as suggested for hydrofracturing. In particular, *Bui* [1998] states that his model applies if the radius of curvature of the bubble, R_c, reaches molecular dimensions, and that is the case for hydrofracturing in rocks. The formula for that curvature is

$$R_c = \frac{4K_{1C}^2(1-\nu^2)^2}{\pi E^2}, \qquad (5)$$

where K_{1c} is the fracture strength, ν is Poisson's ratio, and E is Young's modulus. For soft muddy sediments, typically $E = 1$–10×10^5 N m^{-2}, $K_{1c} = 0.1$–10×10^3 N m$^{-3/2}$ [*Johnson et al.*, 2002; *Barry et al.*, 2010], and Poisson's

ratio is 0.5 [*L'Esperance*, 2009], where the larger values of K_{1C} are associated with the large values of E and the smaller values of K_{1c} are associated with the smaller values of E. Thus R_c is calculated to be of the order of 10^{-6} to 10^{-3} m. These values are 3–6 orders of magnitude larger than the molecular scale considered by *Bui* [1998] (i.e., 5 Å). The model advanced by *Bui* [1998] does not apply in the case of soft sediment (or gelatin).

[23] Finally, bubbles in soft sediments differ from the cracks created by hydrofracturing in three important ways: (1) Gas bubbles do not contain a fluid with an appreciable viscosity (gas versus water); (2) mathematically speaking, hydrofracturing is the propagation of an edge crack, not the growth of a "coin" shaped crack; and (3) soft sediment can and does behave differently than rigid rock to the stresses that create bubbles.

2.2. Nature of Buoyancy in a Solid

[24] The above LEFM growth model describes a bubble in a sediment surrounded by a constant ambient pressure field. To describe rise, however, we need to take into account the fact that the ambient pressure field is not constant but rather increases with depth. The difference in pressure at the top and bottom of the bubble, combined with the difference in density between the bubble fluid (methane) and surrounding medium (bulk sediment), results in the development of a pseudobuoyant force [*Weertman*, 1971a, 1971b]. The magnitude of this force grows as the bubble grows and can eventually cause the bubble to rise through the sediment by steadily propagating a fracture without the need of any additional gas. *Weertman* [1971a] was the first to describe the shape of a 2-D fluid-filled crack in the presence of a pressure gradient, and his theory was used to describe magma transport in ocean crust and propagation of water-filled crevasses in glaciers [*Weertman*, 1971b]. Subsequently, a number of authors have used LEFM to describe the ascent of magma via the propagation of fractures [*Takada*, 1990; *Heimpel and Olson*, 1994; *Dahm*, 2000; *Menand and Tait*, 2001, 2002; *Rivalta and Dahm*, 2006]. All this work was seriously considered when we developed the model of bubble rise presented below.

[25] Rise of a bubble in a solid (e.g., a sediment) is mechanically different than in a fluid. Since a solid can actively resist stress, a positive buoyant force will not necessarily result in bubble rise. A bubble will only rise if the buoyancy force is strong enough to cause the sediment along the leading edge of the bubble to fail, which can only occur when K_{1c} is exceeded. However, along the lower edge of the bubble, stresses remain below K_{1c}, and in fact, this edge will be forced closed as the expansion along the leading edge causes the stresses along this lower boundary to drop below the elastic restoring force of the sediment. The key to incorporating buoyancy into an LEFM model is to characterize how buoyancy contributes to crack loading and determine the correct stress intensity factor for a bubble in a hydrostatic-lithostatic pressure field.

[26] Following *Weertman* [1971a] and *Takada* [1990], we consider a vertically oriented bubble in a pressure field that is no longer constant but increases linearly with depth; that is,

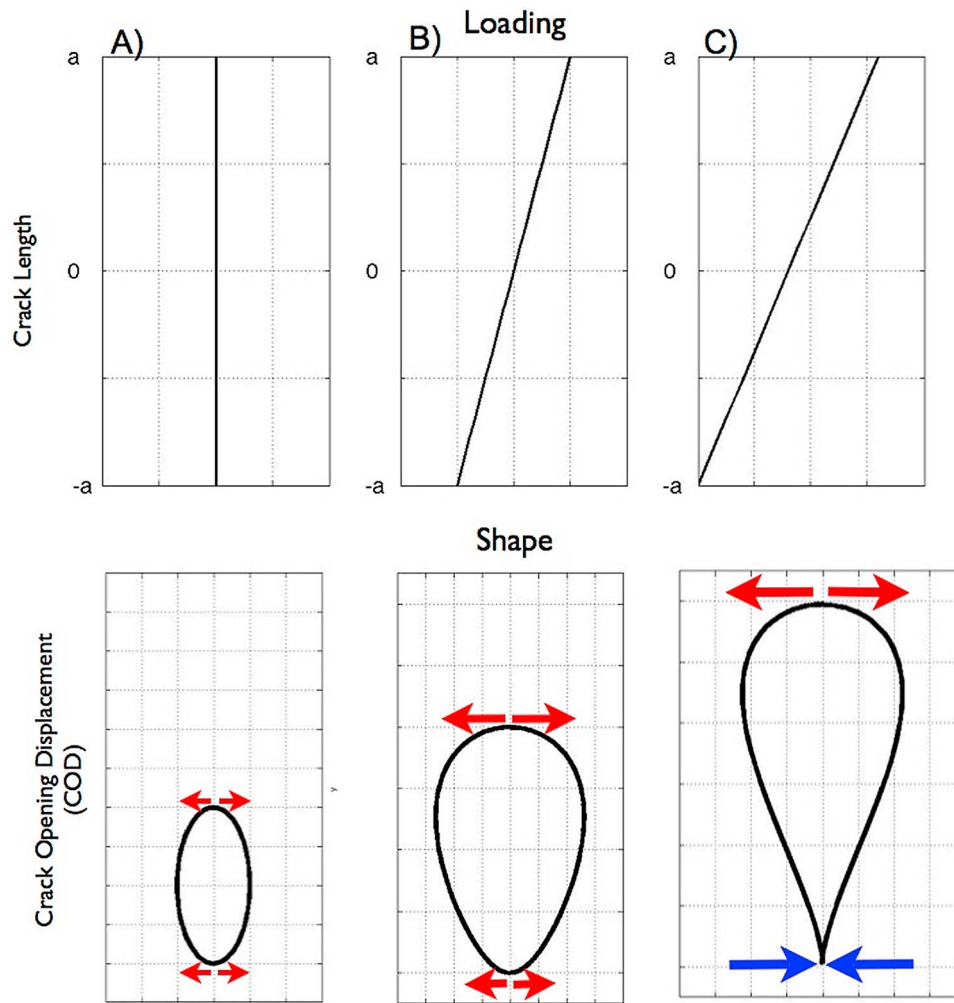$$\sigma(\xi) = \rho_s g'(a + \xi) + \sigma_{-a}, \qquad (6)$$

Figure 6. Schematic diagram of the loading and shape of a vertically oriented crack in a lithostatic-hydrostatic pressure field. (a) At small sizes the difference in pressure between the tip and tail of the bubble is small relative to the internal bubble pressure, and the loading can be considered constant along the length of the crack. (b) As the bubble grows, this pressure difference becomes greater, and the bubble shape deviates from an oblate spheroid. (c) At the point of rise the bubble adopts a teardrop shape, and the loading drops to zero at the crack tail. Any increase in crack length results in the development of compressive stresses in the region of the crack tail, forcing the tail closed. Red arrows represent tensile stresses and blue compressive stresses. The bubble width is grossly exaggerated to show these effects.

where σ is the bubble pressure in excess of ambient pressure, a.k.a. the loading; ξ is a coordinate that describes the position along the crack length ($2a$), which is oriented in the vertical direction, z, with its origin at the center of the bubble; $g' = g(\rho_s - \rho_b)/\rho_s$ (i.e., reduced gravity), where ρ_s is the bulk density of the sediment-pore water continuum; ρ_b is the density of the gas in the bubble; g is the gravitational acceleration; and σ_{-a} is the internal bubble pressure, in excess of ambient pressure, at the crack tail. Provided $\rho_s \gg \rho_b$, as is the case for a methane bubble, g' can be taken to be simply g.

[27] The evolution of the shape and loading of a vertically oriented, growing bubble is shown in Figure 6. Initially the crack length of the bubble is small; the pressure difference between the top and bottom of the bubble is also small and can be ignored, to first order. The loading can be taken as constant along the entire length of the bubble. However, as the bubble grows, the vertical pressure difference begins to manifest itself, as is shown in Figure 6b. The bubble shape begins to deviate from an idealized oblate spheroid, and the tensile stresses concentrated at the crack tip become larger than those at the crack tail. This means that a fracture will always be initiated preferentially at the upper crack tip (edge) and will propagate upward, rather than in both directions. As the crack length grows, the pressure difference between the tip and tail continues to increase; eventually the tensile loading (stress) at the crack tail drops to zero as the internal bubble pressure equals the compressive stresses in the surrounding sediments. At this point the bubble adopts the teardrop shape shown in Figure 6c [*Weertman*, 1971a], and any fracture initiated at the crack tip results in the development of compressive stresses at the
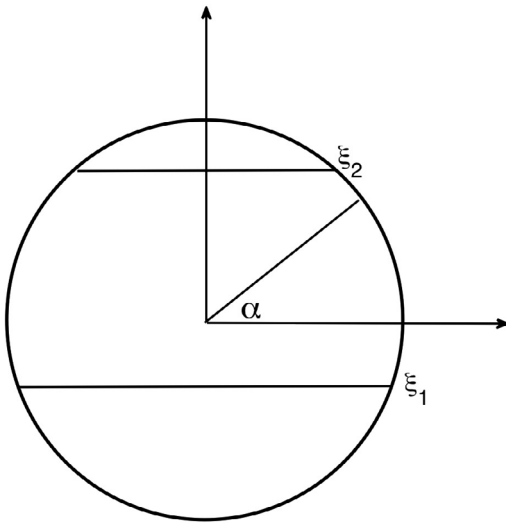
Figure 7. Region of integration for equation (7), where a polynomial load acts on the crack face of a penny-shaped crack from the integration limits ξ_1 to ξ_2.

crack tail, forcing it closed. This closure of the crack tail maintains the crack length and internal pressure, causing the bubble to rise upward, all the while preserving the bubble shape and size.

2.3. K_1 of a Crack Under Buoyant Loading

[28] To quantify the rise mechanism described above, an expression for the stress intensity factor is needed. *Hand* [1992] provides an equation for calculating the stress intensity factor for a penny-shaped crack, subject to a polynomial load varying over the length of the crack. For a load, $F(\xi)$, acting from ξ_1 to ξ_2 (Figure 7), along the circumference of the crack, K_1 is given by

$$K_1(\alpha) = \frac{1}{(\pi a)^{1/2}} \left\{ \int_{\xi_1}^{a\sin\alpha} F(\xi) \left[\frac{(2a)^{1/2}}{(a\sin\alpha - \xi)^{1/2}} \right.\right.$$
$$\left. \cdot \cos\left(\frac{\pi}{4} - \frac{\alpha}{2}\right) - 1 \right] d\xi + \int_{a\sin\alpha}^{\xi_2} F(\xi)$$
$$\left. \cdot \left[\frac{(2a)^{1/2}}{(\xi - a\sin\alpha)^{1/2}} \sin\left(\frac{\pi}{4} - \frac{\alpha}{4} - 1\right) \right] d\xi \right\}. \quad (7)$$

[29] For the buoyant loading given in equation (7), K_1 varies over the circumference of the crack. The highest value occurs at the crack tip ($\alpha = \pi/2$), and the lowest value occurs at the crack tail ($\alpha = -\pi/2$). Substituting $\alpha = \pi/2$ into equation (7) shows that the stress intensity factor at the crack tip, $K_1^{(+)}$, is given by the first integral only,

$$K_1^{(+)} = K_1\left(\frac{\pi}{2}\right) = \frac{1}{(\pi a)^{1/2}} \int_{-a}^{a} \rho_s g(a - \xi) \left[\frac{(2a)^{1/2}}{(a - \xi)^{1/2}} - 1 \right] d\xi, \quad (8)$$

and upon integration this yields

$$K_1^{(+)} = \frac{10}{3\pi} \rho_s g a \sqrt{\pi a}. \quad (9)$$

[30] For the crack tail, $\alpha = -\pi/2$, only the second integral in equation (7) is nonzero, and $K_1^{(-)}$ is given by

$$K_1^{(-)} = K_1\left(-\frac{\pi}{2}\right) = \frac{1}{(\pi a)^{1/2}} \int_{-a}^{a} \rho_s g(a - \xi) \left[\frac{(2a)^{1/2}}{(a + \xi)^{1/2}} - 1 \right] d\xi, \quad (10)$$

which gives, after integration,

$$K_1^{(-)} = \frac{2}{3\pi} \rho_s g a \sqrt{\pi a}. \quad (11)$$

[31] For a small bubble the stress intensity factor is still given by equation (1). For a bubble of intermediate crack length, Figure 6b, K_1 at the crack tip is found by superposition of equations (1) and (8),

$$K_1^{(+)} = \frac{10}{3\pi} \rho_s g a \sqrt{\pi a} + \frac{2}{\pi} \sigma_{-a} \sqrt{\pi a}, \quad (12)$$

where σ_{-a} is the loading at the crack tail.

2.4. Criterion for Initial Rise

[32] Equation (12) is the general expression for K_1 that accounts for buoyancy. As the crack grows, the contribution from the first term in equation (12) at fracture ($K_1 = K_{1c}$) increases until a crack length is reached where only the first term is needed to equal K_{1c}; this is the bubble depicted in Figure 6c, and at this size the bubble will rise. The crack length at which this occurs, a_r, is found by rearranging equation (12) and setting K_1 to K_{1c},

$$a_r = \left(\frac{3K_{1c}\sqrt{\pi}}{10\rho_s g} \right)^{2/3}, \quad (13)$$

where a_r is a material property, and this size constitutes the bubble rise criterion. A similar equation with slightly different numerical constants is reported by *Weertman* [1971a, 1971b] and *Rivalta et al.* [2005].

[33] The point in time at which the bubble begins to rise is determined by the long axis of the bubble only, rather than by the entire volume, such as in the case for a true buoyant force. For this reason *Weertman* [1971a] terms the driving force of a buoyant crack a pseudobuoyant force. The volume of a bubble, when the critical crack length is reached, is determined by the amount of elastic expansion of the bubble walls and is dependent on both Poisson's ratio and Young's modulus, according to the crack opening displacement (COD) formula, which, for a linear load, is given by *Sneddon* [1946] as

$$b(z,x) = \frac{4(1 - \nu^2)}{\pi E} (\rho_s g a + \sigma_{-a}) \sqrt{a^2 - z^2 - x^2}. \quad (14)$$

The volume of a bubble when it begins to rise can then be found by setting σ_{-a} to 0 and integrating the COD formula over the entire surface of the bubble, where the position on the surface of the bubble is expressed in polar coordinates with the origin at the center of the crack plane,

$$V_b = \frac{(1 - \nu^2)}{\pi E} \int_0^{2\pi} \int_0^a \rho_s g r^2 \sqrt{a^2 - r^2} \, dr d\theta = \frac{16(1 - \nu^2)\rho_s g a^4}{3E}. \quad (15)$$
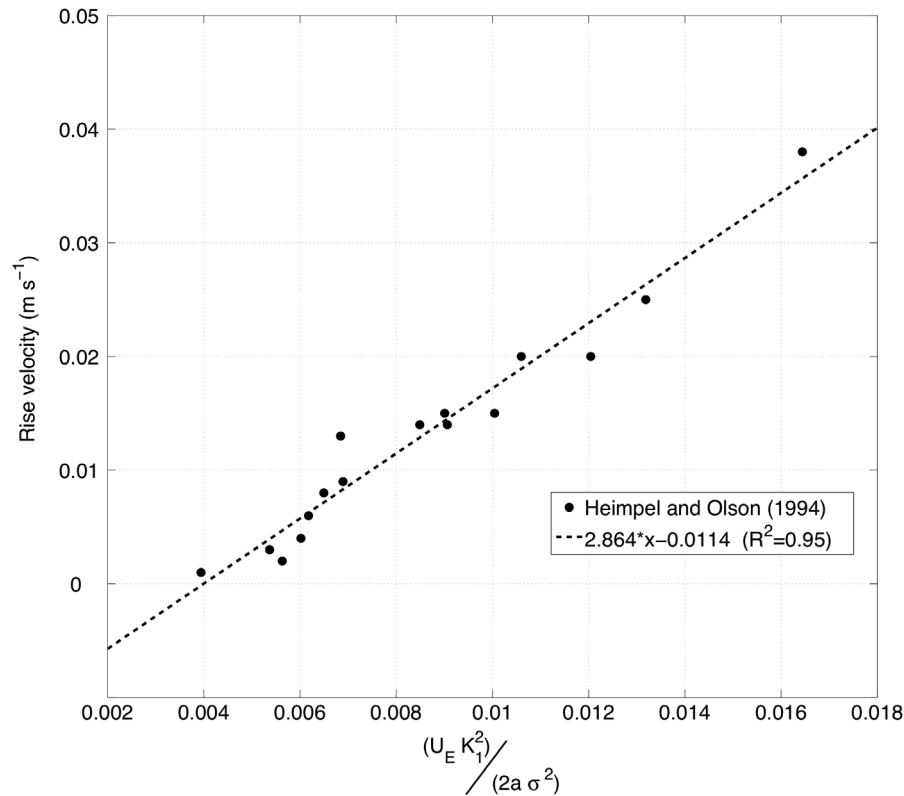
Figure 8. A comparison of the bubble rise velocities from *Heimpel and Olson* [1994] and the velocities predicted from equations (16) and (17), U_F. The values for K_1 and the yield stress, σ_y, were also taken from *Heimpel and Olson* [1994].

[34] If the mechanical parameters from *Johnson et al.* [2002] are entered into equation (15), i.e., $E = 1.4 \times 10^5\ \mathrm{Nm}^{-2}$ and $K_{1c} = 300\ \mathrm{Nm}^{-3/2}$, and $\nu = 0.5$ [*L'Esperance*, 2009], the critical volume of rise is $4\ \mathrm{cm}^3$, corresponding to a critical crack length of 10 cm. This crack length is close (within a factor of 2) to that of the largest bubbles observed using X-ray scans of box cores from Cape Lookout Bight, a productive estuary on the Outer Banks of North Carolina, where bubble ebullition is known to occur [*Martens and Klump*, 1980].

3. Mechanics of Initial Bubble Rise

[35] The rise of a buoyant body in a solid has been considered in the fields of magma rise and hydrofracturing [e.g., *Weertman*, 1971b; *Heimpel and Olson*, 1994; *Dahm*, 2000; *Menand and Tait*, 2002; *Rivalta and Dahm*, 2006]. Two mechanical models have been championed with respect to controlling the rise speed of a buoyant body/fluid rise in geophysical solids: (1) One is the rate of transfer of information via a Rayleigh wave traveling from the top to the bottom of the rising body [*Heimpel and Olson*, 1994], and (2) the other is the rate of the movement of the internal fluid (e.g., magma, water) into the newly opened fracture; this would be controlled by the viscosity and flow regime of the fluid [*Weertman*, 1971b; *Dahm*, 2000].

[36] The first of these possibilities assumes elastically controlled buoyant crack propagation and is summarized nicely by *Heimpel and Olson* [1994]; these authors state that the rise velocity is controlled by the dynamical constraint

that fracture at the crack tip is matched by closure at the crack tail, maintaining loading at a time-averaged steady state and preserving the bubble shape in Figure 6c. This ensures that inertial terms, such as the dynamic stress intensity factor [*Freund*, 1990], can be neglected. Instead, the rise velocity, U_F, is controlled by the lag time between crack propagation at the crack tip and closure at the tail.

[37] In this purely elastic mechanical model, a fracture will initially propagate the length of the process zone. The process zone is the necessarily small region ahead of the crack tip where plastic deformations may occur and the physical act of bond breaking takes place. There are many different formulas for describing the size and shape of the process zone, but one of the simplest and arguably most widely accepted is the Dugdale zone [*Gross and Seelig*, 2006]; that is,

$$d = \frac{\pi}{8}\left(\frac{K_{1c}}{\sigma_y}\right)^2, \qquad (16)$$

where d is the length of the process zone and σ_y is the yield strength of the solid (sediment). Crack propagation the length of this zone causes the bubble volume to increase and the crack loading to decrease below K_{1c} until the crack tail closes, returning the load to the original level. The crack propagation velocity is therefore constrained by the time it takes information about the crack opening to travel to the crack tail. This information travels at the Rayleigh wave speed, U_R, of the material [*Gross and Seelig*, 2006]. This speed, depends on the value of Poisson's ratio and the shear wave velocity

Table 2. Parameter Values Used in Bubble Growth Simulations, Chosen to Correspond to Conditions at Cape Lookout Bight, North Carolina

Name	Symbol	Value
Young's modulus	E	1.4×10^5 Nm^{-2}
Poisson's ratio	ν	0.3
Fracture toughness	K_{1c}	300 Nm$^{-3/2}$
Sediment viscosity	η	21,400 Pa s
Bulk sediment density	ρ_s	1,200 kg m^{-3}
Yield strength	σ_y	2,000 Nm^{-2}
Temperature	T	293 K

of the material, U_E; specifically, for sediment with $\nu = 0.5$ [*L'Esperance*, 2009], $U_R = 0.955U_E$. The shear wave velocity of sediments has been widely measured [e.g., *Hamilton*, 1976; *Matthews*, 1982; *Gabriels et al.*, 1987; *Holzer et al.*, 2005] and is of the order of 100 m s^{-1} for surface sediments. Therefore $U_E = 96$ m s^{-1} in sediments to first-order accuracy.

[38] The expression for elastically controlled rise of a bubble now gives that

$$U_F = \frac{d}{\tau_f} = \frac{U_E d}{2a}, \qquad (17)$$

where $\tau_f = 2a/U_E$ is the time required for information to travel from crack tip to crack tail. A comparison of equation (17) to bubble rise data in gelatin from *Heimpel and Olson* [1994] (see Figure 8) reveals a linear relationship, suggesting that this model adequately predicts rise velocities in that material, at least as a first-order approximation.

[39] With these expressions, a time scale for the rate of elastic rise can be established. The elastic parameters of Table 2, a shear wave velocity of 96 m s^{-1} and $a = a_r = 0.05$ m, produce together a time scale of $\sim 5 \times 10^{-4}$ s. For a process zone of 1 mm to 1 cm (i.e., yield strength from 2000 Nm^{-2} to 5000 Nm^{-2}), this gives a rise velocity ranging from 2 to 20 m s^{-1}. This range represents unreasonably rapid rises (i.e., ballistic at the high end) and must be considered an upper limit on possible rise velocity. No one in the literature has reported bubbles shooting out of sediments. There are no data on rise speeds in sediments, but these calculated values are much greater than speeds observed in gelatin (Figure 8). We believe that real bubble velocities in sediments are considerably lower than this limit.

[40] Various authors have developed models based on the mechanism of point 2 "dry" above, wherein the viscosity of the fluid within the crack/bubble controls the speed of fracture propagation [*Dahm*, 2000; *Weertman*, 1971b], and such models have been applied to describe the ascent of magma by dyke propagation. While this makes sense for an extremely viscous fluid like magma (i.e., $\eta \approx 10^4$ Pa s), it is unlikely that this could control the rise of a gas-filled ("dry") bubble with gas viscosity 9 orders of magnitude lower (i.e., $\eta \approx 10^{-5}$ Pa s). Why? Because the speed of fluid movement in the new propagated crack is roughly proportional to the inverse of that fluid's viscosity; thus, the speed of gas movement in a crack is roughly 9 orders of magnitude faster than that of magma (and 2 orders of magnitude faster than water.) Therefore it is our contention that the viscosity of the fluid (i.e., the gas) is not controlling the rise velocity of a bubble in soft sediment.

[41] If the two previously stated mechanical models do not afford good explanations for the rise of bubbles in soft sediments, does there exist a third and unconsidered alternative? Yes. The stress response of the soft sediment cannot
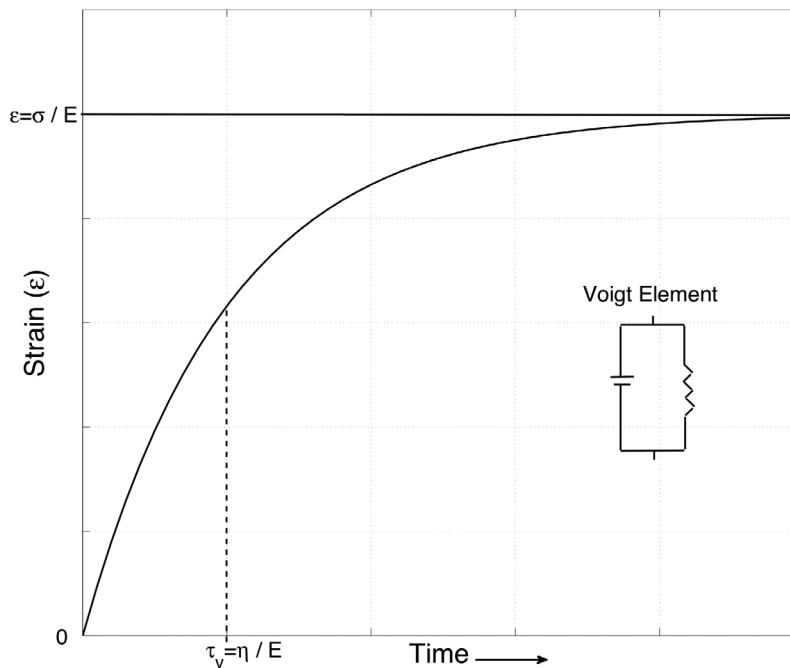

Figure 9. The time-dependent strain curve of a Voigt body subjected to constant loading, σ. The viscoelastic Voigt model can be visualized as a spring and a dashpot, connected in parallel (inset). Initially, the material experiences no strain, as the dashpot resists any movement. At long times the strain is equal to the elastic solution for an equivalent loading. The response time is given by the ratio between the spring constant (Young's modulus) and the viscosity of the dashpot, $\tau_v = \eta/E$.

Table 3. Rise Velocities for Some Mud Viscosities Reported in the Literature

Viscosity (Pa s)	Stress Response Time $\tau_\nu = \eta/E$ (s)	Rise Velocity (cm s^{-1})
225[a]	0.0016	47
800[b]	0.0057	22
21,400[a]	0.15	0.8
140,000	1	0.2

[a]Data from *Jiang and Mehta* [1995].
[b]Data from *Hsiao and Shemdin* [1980]. E is set to 1.4×10 Nm^{-2}, and $\nu = 0.3$.

be instantaneous, as in the linear elastic growth models [e.g., *Algar and Boudreau*, 2009; *Gardiner et al.*, 2003]; instead, there should be a time-dependent viscoelastic response. The sediment can then be treated as a Voigt material, which can be represented schematically by a spring and damper (dashpot) connected in parallel (Figure 9). Why a Voigt material? The fact that bubbles obtain a stable shape and are explained fully by LEFM (Figure 5) indicates that muddy sediment over time scales of hours to days (and maybe weeks to months) act as elastic solids. The bubbles do not deform with time (i.e., creep) and do not become more spherical, as would be expected if the sediment was a fluid over longer time periods.

[42] We need to add viscosity to introduce a "short" time scale to the model that accounts for the fact that sediment cannot instantaneously move out of the way of a growing or rising bubble. This viscosity has no effect on the ultimate shape of a bubble (Figure 5), so LEFM describes the final stable state well; thus, a "short" timescale of flow coupled to longer-term elastic behavior equals a Kelvin-Voigt solid (material).

[43] A Kelvin-Voigt model may, at first, seem an odd choice when soft sediments are known to transmit shear waves [e.g., *Hamilton*, 1976], but there is, in fact, nothing eccentric in this. Depending on the magnitude of the applied stress and its rate of application, sediments can respond in a variety of ways. To acoustic stresses, sediments are adequately characterized as elastic [*Hamilton*, 1980], although recent acoustic interpretations use more complicated models. To bubble and animal induced stresses, clay-bearing sediments appear to be either elastic or viscoelastic [*Johnson et al.*, 2002; *Dorgan et al.*, 2005; *Barry et al.*, 2010]. Yet when a sediment fails and fluidizes during seismic activity, the sediment might be described as a Maxwell material. When one observes one's, apparently stable, footprints in the mud of a marsh or mud flat, the notion of plasticity comes to mind. Without doubt, sediments are far more complex than our simple, end-member, idealized behaviors can capture. Sediments can be said to be viscoelastic-plastic materials, but that does not mean that a simple model might not adequately account for the changes (strains) caused by a limited range of stress and stress rate. Thus, for the bubbles grown at the rates and sizes discussed in this paper and our past papers, a Voigt model is a reasonably accurate description. (Caveat emptor when blindly applied to some other process.)

[44] The stress-strain relationship now takes the form:

$$\sigma(t) = E\varepsilon(t) + \eta\frac{d\varepsilon(t)}{dt}, \qquad (18)$$

where η is the viscosity of the sediment that dampens the elastic response. Figure 9 also shows the stress response of a Voigt material to a constantly applied load. Notice that the system ultimately obtains the same degree of strain as in the elastic case, but the response is now associated with a time constant; that is,

$$\tau_\nu = \frac{\eta}{E}. \qquad (19)$$

[45] A comparison of τ_ν to the time scale of the elastic response for a Young's modulus of $E = 1.4 \times 10^5$ Nm^{-2} and a fracture toughness of $K_{1c} = 300$ Nm$^{-3/2}$ shows that τ_ν becomes significant when $\eta > 350$ Pa s. For sediment viscosities smaller than this, the response can be assumed to be entirely elastic. Table 3 shows several mud viscosities taken from *Hsiao and Shemdin* [1980] and *Jiang and Mehta* [1995] with η ranging from 225 to 140 000 Pa s, which corresponds to a viscoelastic response time from 0.0016 to 1 s, suggesting that viscoelastic behavior largely controls bubble rise.

4. A Viscoelastic-Fracture Bubble-Rise Model

[46] To model bubble rise, we offer a new mechanical model that captures the viscoelastic-fracture behavior of sediments. This model is solved within in a commercially available, finite element modeling software package, Comsol Multiphysics®. Only the mechanics of rise are modeled; gas production and mass transfer between the rising bubble and surrounding sediments are not taken into account. The latter of these processes is ignored because the time scale of diffusional transport, days to weeks [*Algar and Boudreau*, 2009] (see section 5), is generally much longer than the time scale of rise, meaning that the mass of the bubble is essentially conserved during rise.

[47] Our new model considers a single isolated bubble in an otherwise undisturbed region of sediment. This model does not consider the rise of bubbles through already formed bubble tubes/long fractures to the surface, but rather describes the initial rise of a single bubble in an homogeneous sediment characterized by a K_{1c} value. The fracture path thus created can provide a fracture path along which other bubbles may later follow, a process that could eventually create a bubble tube. The geometry for the model is shown in Figure 10. Owing to symmetry, only half the bubble/sediment domain needs to be modeled. The model consists of a column of sediment with a bubble represented by an oval surface at the midpoint of one side of the domain.

[48] The opening and closing of the crack tip is modeled by calculating the displacement of the surrounding sediment as a result of the stresses induced by the internal bubble pressure. The resulting displacements are obtained by solving the elasticity equation for a three-dimensional body; that is,

$$\rho_s\frac{\partial^2\mathbf{u}}{\partial t^2} = \nabla \cdot c\nabla\mathbf{u} \qquad (20)$$

where $\mathbf{u}$ is a vector of the displacements in the x, y and z directions and c is the elasticity tensor as described by *Timoshenko and Goodier* [1970].

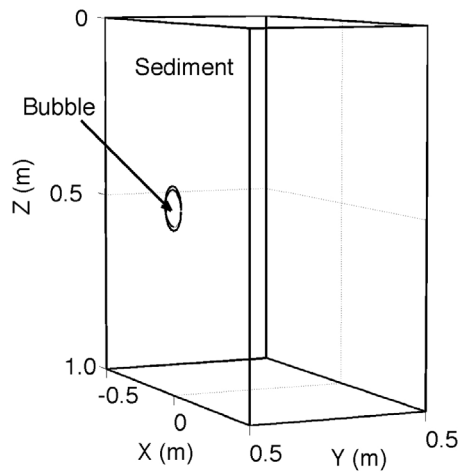[49] The internal bubble pressure appears as a boundary load on the bubble surface, in the same manner as in the

Figure 10. Geometry of the 3-D linear elastic fracture mechanics bubble rise model. Because of symmetry, only one half of the sediment/bubble domain needs to be modeled.

work of *Algar and Boudreau* [2009], but now the ambient pressure is an increasing linear function of depth,

$$-\mathbf{n} \cdot c\nabla\mathbf{u} = \psi_b RT - P_{sw} - \rho_s gz \qquad (21)$$

where ψ_b is the methane concentration inside the bubble, R_g is the ideal gas constant, T is the temperature, P_{sw} is the hydrostatic pressure at the sediment water interface, and $\mathbf{n}$ is the outward normal unit vector.

[50] The volume of the bubble, V_b, is obtained by integrating the displacements along the bubble surface,

$$V_b = 2 \int_{S=\alpha_0} \mathbf{n} \cdot \mathbf{u} dS, \qquad (22)$$

where α_0 represents the bubble surface and the factor of 2 is present because only half the bubble is being measured. The internal gas concentration of the bubble is then calculated as

$$\psi_b = \frac{N}{2 \int_{S=\alpha_0} \mathbf{n} \cdot \mathbf{u} dS}, \qquad (23)$$

where the denominator is the bubble volume and N is the number of moles of gas in the bubble, which stays constant thought the rise simulation. Note that it is the mass, and not the volume, that is held constant throughout a simulation.

[51] The Voigt material viscosity is incorporated into the model by modifying the Rayleigh dampening equation included in the mechanics of the COMSOL Multiphysics® stress/strain module, which solves equations (20) through (23). In finite element formulation the model takes the form

$$[\mathbf{M}]\{\ddot{\mathbf{u}}(t)\} + [\mathbf{C}]\{\dot{\mathbf{u}}(t)\} + [\mathbf{K}]\{\mathbf{u}(t)\} = \{\mathbf{F}\} \qquad (24)$$

with

$$[\mathbf{C}] = \alpha_M[\mathbf{M}] + \beta_K[\mathbf{K}], \qquad (25)$$

where $[\mathbf{K}]$ is the stiffness matrix, $[\mathbf{M}]$ is the mass matrix, $\{\mathbf{F}\}$ is the vector of body forces, and $[\mathbf{C}]$ is the damping

matrix. The α_M and β_K are dampening constants. The Voigt material is created by setting $\beta_K = \eta/E$ and α_M to a very small number ($\alpha_M \rightarrow 0$).

[52] The traditional view of LEFM theory assumes fracture propagation occurs when $K_1 = K_{1c}$, according to equation (1). However, in the viscoelastic model, the stresses and strains are no longer in phase, so this approach is not valid. Instead, the concept of a critical crack tip opening displacement (CTOD) is used [*Gross and Seelig*, 2006]. The CTOD is the crack opening displacement at an angle originating at the crack tip and 45° from the crack plane (Figure 11). Fracture occurs when CTOD achieves a critical value. For elastic conditions the K_{1c} and the CTOD approaches are equivalent. For the viscoelastic bubble rise model the CTOD approach was used to characterize the onset of each fracture event. (Note that CTOD should not be confused with crack opening displacement (COD). COD refers to the opening along the entire length of the crack, while CTOD refers to the crack opening at a single point near the crack tip.)

[53] To capture a fracture event, the bubble surface is first advanced by the length of the process zone; then the time-dependent stress-strain equations, with a viscosity term included, are solved with the displacements from the previous fracture event used as initial conditions. This procedure calculates the movement of the bubble walls during a fracture event, and this approach is repeated to capture the opening of each successive fracture event as the bubble travels upward through the sediment.

5. Model Results and Discussion

[54] Our finite element viscoelastic bubble-rise model calculates the stresses and strains in the sediments surrounding a bubble as it rises. Figure 12 illustrates the stresses surrounding a rising bubble. Note that the crack opening displacement, COD, has been exaggerated by a
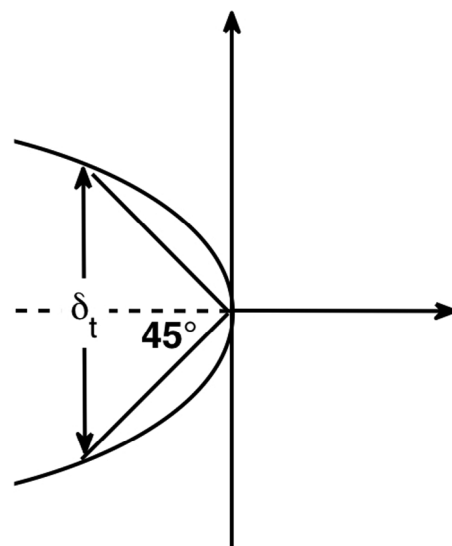

Figure 11. The crack tip opening displacement (CTOD) is the crack opening displacement at an angle initiating at the crack tip and 45° from the plane of the crack. Fracture propagation occurs when CTOD obtains a critical value, δ_t.
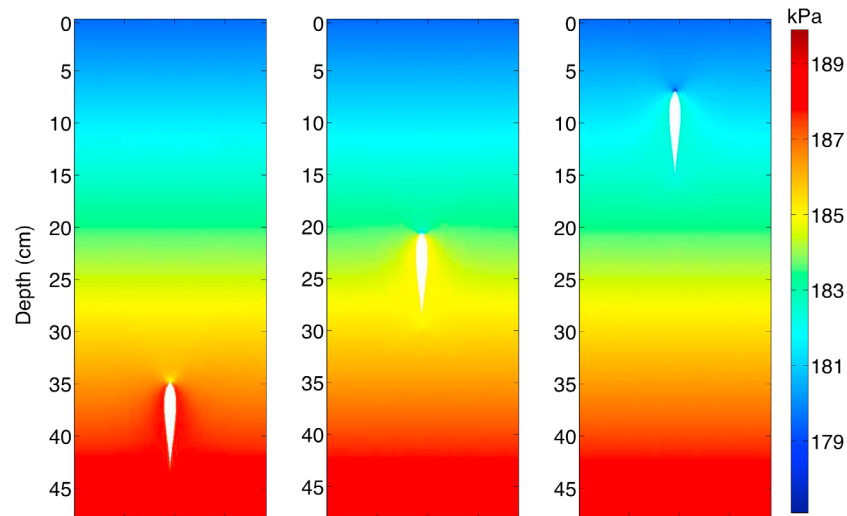
Figure 12. Stresses surrounding a rising bubble at three points during a model simulation. Along the outer boundary of the model, stress increases linearly with depth, while at the bubble tip the stresses induced by the bubble are visible. The horizontal displacement of the bubble walls has been exaggerated by a factor of 10, so that the teardrop shape of the bubble can be clearly seen.

factor of 10, so that the teardrop shape of the fracture can be more easily seen. In the region near the bubble, the concentrated tensile stresses at the crack tip are visible, as well as a smaller region of compressive stresses at the crack tail. This is more easily seen in Figure 13, which shows only the bubble-induced stresses at various stages of crack opening, along with the displacements of the bubble walls.

[55] Model runs were carried out with the viscosities in Table 3, using the values of E and ν in Table 2 for sediments; then, by plotting the position of the crack tip with time, an average rise velocity can be obtained. The velocities for each of these simulations are also shown in Table 3 and are of the order of centimeters per second. Figure 14 shows an example of the position of the crack tip with time throughout a simulation. Least squares analysis is used to calculate the velocities. Notice that the velocity remains constant throughout the entire period of rise. This is consistent with bubble rise in gelatin; that is, see *Rivalta et al.* [2005], who also report constant rise velocities throughout the duration of their experiment.

[56] Nevertheless, *Rivalta and Dahm* [2006] examined the behavior of bubbles as they approach a boundary or free surface and found that bubbles accelerate as the boundary is approached. This is not captured in the model as the boundary conditions and resolution do not account for this detail. As this only occurs in the immediate vicinity of the boundary, it would not have a significant effect upon the average rise velocity or time scale of release.

[57] To understand why ebullition is an efficient methane transport mechanism compared to diffusion, the time scales of release of gas from sediment by bubble rise and dissolved-gas diffusion can be compared. For productive estuarine and lake environments, methane concentrations often reach supersaturation within 10–30 cm of the sediment-water interface [e.g., *Martens and Klump*, 1980]. Using this range of depths as maximum and minimum length scales and the maximum and minimum viscosities of Table 3, it can be seen that it takes anywhere from a few

seconds to a few minutes for a bubble to rise initially from the region of supersaturation through the methane oxidizing zone. Contrast this to the time scale of diffusion, which can be calculated using Einstein's relation,

$$\tau_D = \frac{L^2}{D}. \tag{26}$$

For $D = 1.33 \times 10^{-9}$ m^{-2} s^{-1} [*Boudreau*, 1997] and $L = 0.1$ to L = 0.3 m, equation (26) gives a time scale of the order of weeks to months for methane to pass through the oxidizing zone. Ebullition can therefore move bubbles rapidly through this zone, limiting the amount of oxidative loss. Conversely, much of the diffusive flux is consumed.

[58] It is important to stress that the rise mechanism presented here is not meant to describe all sediment environments, but is restricted to those that display fracture behavior, although it appears that this represents a significant portion of the sediments that house gas bubbles. At this point some mention of the presence of bubble tubes in many sediments with high bubbling rates must be made. Fractures, left over from the rise of previous bubbles, which have closed but only partially healed become planes of weakness, along which other bubbles may potentially rise, and the reason bubbles preferentially rise in regions where other bubbles have previously risen [*Martens and Klump*, 1980]. Bubble tubes may form as result of each passing bubble resuspending small amounts of sediment [*Klein*, 2006], until enough sediment has been removed to create a permanent tube structure. However, the existence of such tubes could likely indicate that these sediments are behaving plastically. It is possible that uppermost sediments, with the greatest water contents, do not follow LEFM but rather respond plastically; if this is the case, a Maxwell model for the stress response, with failure according to the Mohr-Coulomb criteria, might be a more appropriate model for these sediments, with a transition to LEFM behavior at depth as water contents decrease and the sediments become stiffer.

[59] Such a transition emphasizes the need to better characterize the rheology of gassy sediments. Once this is achieved, models such as the one presented here, will be better constrained and provide more accurate estimates of rise velocities. Finally, although in this work we have examined shallow-water sediments, with confining pressure of the order of 200–300 kPa, this theory of rise could also be applied to deeper sediments with higher confining pressures, such as the hydrate stability zone. Our model could aid in the understanding of gas migration to and from regions of hydrate formation.

6. Conclusions

[60] According to our LEFM-based theory, bubbles rise when the long axis of the bubble reaches a critical length, a_r, and this is determined by the fracture toughness of the sediment. The lower the fracture toughness, the smaller a bubble will be when it begins to rise. We have also shown that capillary pressure plays no role in controlling the ini-
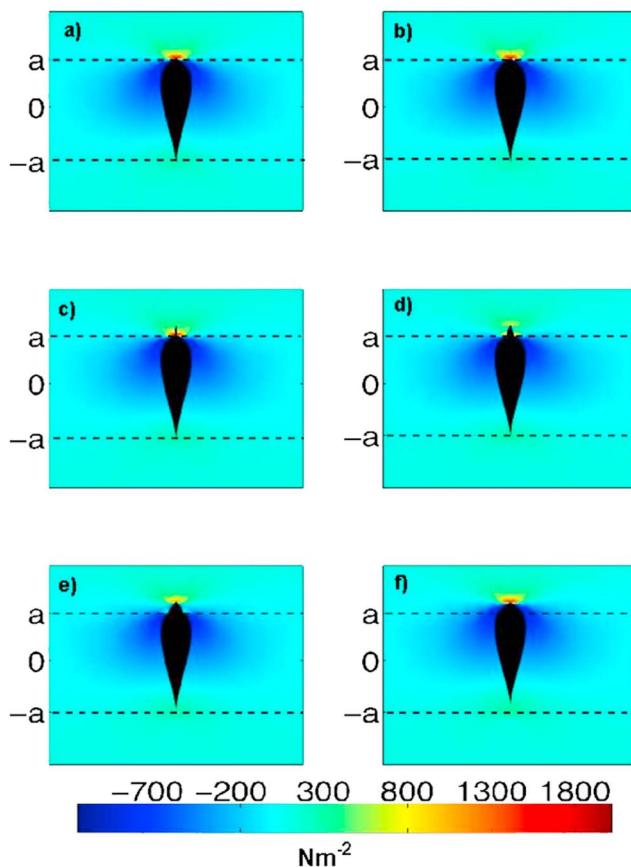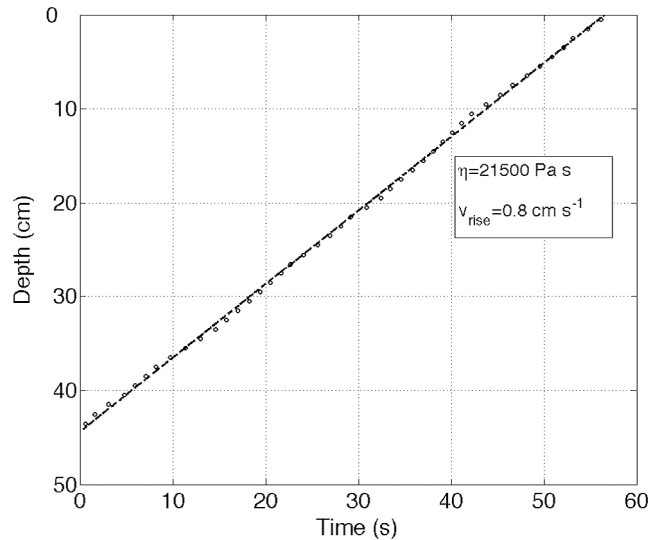

Figure 14. An example of a rise simulation showing the position of the crack tip with time at the beginning of each fracture event. Parameters used were $E = 1.4 \times 10^5$ Nm^{-2}, $\nu = 0.3$, $\eta = 21,500$ Pa s, $a_r = 0.05$ m, and $K_{1c} = 300$ $Nm^{-3/2}$. The open circles are the position of the crack tip with time, and the dashed line is the least squared analysis used to calculate the rise velocity. The slight fluctuations in the crack tip position are an artifact of the model and could be eliminated with a smaller time step, but this significantly slows down the solution time, with little effect on the calculated rise velocity and so was not done.

tiation of rise, even if it is essential in the coherence of a bubble.

[61] The speed of rise is controlled by the lag time between opening of the crack tip and closure at the crack tail. Linear elastic behavior constrains the upper limit of the rise velocity; however, the viscoelastic properties in Tables 2 and 3 indicate that viscoelastic behavior controls rise in most sediments; on the basis of this fact, we estimate rise velocities of the order of centimeters per second.

Figure 13. Fracture propagation during bubble rise, showing both opening at the crack tip and closure at the tail, and the stresses induced by the bubble in the surrounding sediments. Negative values indicate compressive stresses, and positive values indicate tensile stresses. The dotted lines indicate the position of the crack tip and tail at the onset of fracture propagation. The displacements of the bubble walls have been exaggerated by a factor of 50 so that the shape of the fracture can be easily seen. (Note that 1 N m^{-2} = 1 Pa.)

References

Abegg, F., A. Anderson, L. Buzi, A. P. Lyons, and T. H. Orsi (1994), Free methane concentration and bubble characteristics in Eckernförde Bay, Germany, in *Proceedings of the Gassy Mud Workshop*, edited by T. F. Wever, pp. 84–89, Forsch. der Bundeswehr für Wasserschall- und Geophys. (FWG), Bonn, Germany.

Algar, C., and B. P. Boudreau (2009), Transient growth of an isolated bubble in muddy, fine-grained sediments, *Geochim. Cosmochim. Acta*, 73, 2581–2591, doi:10.1016/j.gca.2009.02.008.

Anderson, A. L., F. Abegg, J. A. Hawkins, M. E. Duncan, and A. P. Lyons (1998), Bubble populations and acoustic interaction with the gassy floor of Eckernförde Bay, *Cont. Shelf Res.*, 18, 1807–1838, doi:10.1016/S0278-4343(98)00059-4.

Barry, M. (2010), Elastic and fracture behaviour of marine sediment in response to free gas, Ph.D. thesis, Dalhousie Univ., Halifax, Nova Scotia, Canada.

Barry, M., B. P. Boudreau, B. D. Johnson, and A. H. Reed (2010), First-order description of the mechanical fracture behavior of fine-grained surficial marine sediments during gas bubble growth, *J. Geophys. Res.*, *115*, F04029, doi:10.1029/2010JF001833.

Best, A. I., M. D. J. Tuffin, J. K. Dix, and J. M. Bull (2004), Tidal height dependence of acoustic velocity and attenuation in shallow gassy marine sediments, *J. Geophys. Res.*, *109*, B08101, doi:10.1029/2003JB002748.

Bons, P., and B. Milligen (2001), New experiment to model self-organized critical transport and accumulation of melt and hydrocarbons from their source rocks, *Geology*, *29*, 919–922, doi:10.1130/0091-7613(2001) 029<0919:NETMSO>2.0.CO;2.

Bons, P., and A. Saesoo (2003), Could magma transport and accumulation be a useful analogue to understand hydrocarbon extraction?, *Oil Shale*, *20*, 412–420.

Boudreau, B. P. (1997), *Diagenetic Models and Their Implication*, Springer, New York.

Boudreau, B. P., C. Algar, B. D. Johnson, I. Croudace, A. Reed, Y. Furukawa, K. M. Dorgan, P. A. Jumars, A. S. Grader, and B. S. Gardiner (2005), Bubble growth and rise in soft sediments, *Geology*, *33*, 517–520, doi:10.1130/G21259.1.

Broek, D. (1982), *Elementary Engineering Fracture Mechanics*, 4th ed., Kluwer Acad., Norwell, Mass.

Bui, H. D. (1998), Interaction between the Griffith crack and a fluid: Theory of Rehbinder's effect, in *Fracture: A Topical Encyclopedia of Current Knowledge*, edited by G. P. Chereponov, pp. 99–105, Krieger Publ., Malabar, Fla.

Chanton, J., C. Martens, and C. A. Kelley (1989), Gas transport from methane-saturated, tidal freshwater and wetland sediments, *Limnol. Oceanogr.*, *34*, 807–819, doi:10.4319/lo.1989.34.5.0807.

Dahm, T. (2000), On the shape and velocity of fluid-filled fractures in the Earth, *Geophys. J. Int.*, *142*, 181–192, doi:10.1046/j.1365-246x.2000.00148.x.

Dorgan, K., P. Jumars, B. D. Johnson, B. P. Boudreau, and E. Landis (2005), Burrowing mechanics: Burrow extension by crack propagation, *Nature*, *433*, 475, doi:10.1038/433475a.

Freund, L. (1990), *Dynamic Fracture Mechanics*, Cambridge Univ. Press, Cambridge, U. K.

Gabriels, P., R. Snieder, and G. Nolet (1987), In situ measurements of shear-wave velocity in sediments with higher-mode Rayleigh waves, *Geophys. Prospect.*, *35*, 187–196, doi:10.1111/j.1365-2478.1987.tb00812.x.

Gardiner, B. S., B. P. Boudreau, and B. D. Johnson (2003), Growth of disk-shaped bubbles in sediments, *Geochim. Cosmochim. Acta*, *67*, 1485–1494, doi:10.1016/S0016-7037(02)01072-4.

Gross, E., and T. Seelig (2006), *Fracture Mechanics: With an Introduction to Micromechanics*, Springer, Berlin.

Hamilton, E. L. (1976), Shear-wave velocity versus depth in marine sediments, *Rev. Geophys.*, *41*, 985–996.

Hamilton, E. L. (1980), Geoacoustical modeling of the sea floor, *J. Acoust. Soc. Am.*, *68*, 1313–1340, doi:10.1121/1.385100.

Hand, R. (1992), Stress intensity factors for penny and half-penny shaped cracks subjected to a stress gradient, *Int. J. Fract.*, *57*, 237–247.

Heimpel, H., and P. Olson (1994), Buoyancy-driven fracture and magma transport through the lithosphere: Models and experiments, in *Magmatic Systems*, edited by M. Ryan, chap. 10, pp. 223–240, Academic, San Diego Calif.

Holzer, T. L., M. J. Bennett, T. E. Noce, and J. C. Tinsley (2005), Shear-wave velocity of surficial geologic sediments in northern California: Statistical distributions and depth dependence, *Earthquake Spectra*, *21*, 161–177, doi:10.1193/1.1852561.

Hovland, M., and A. Judd (1988), *Seabed Pockmarks and Seepages: Impact on Geology, Biology and the Marine Environment*, Graham and Trotman, London.

Hsiao, S., and O. Shemdin (1980), Interaction of ocean waves with a soft bottom, *J. Phys. Oceanogr.*, *10*, 605–610, doi:10.1175/1520-0485(1980) 010<0605:IOOWWA>2.0.CO;2.

Jain, A., and R. Juanes (2009), Preferential mode of gas invasion in sediments: Grain-scale mechanistic model of coupled multiphase fluid flow and sediment mechanics, *J. Geophys. Res.*, *114*, B08101, doi:10.1029/2008JB006002.

Jiang, F., and A. Mehta (1995), Mudbanks of the southwest coast of India IV: Mud viscoelastic properties, *J. Coastal Res.*, *11*, 918–926.

Johnson, B. D., B. P. Boudreau, B. S. Gardiner, and R. Maass (2002), Mechanical response of sediments to bubble growth, *Mar. Geol.*, *187*, 347–363, doi:10.1016/S0025-3227(02)00383-3.

Judd, A. (2003), The global importance and context of methane escape from the seabed, *Geo Mar. Lett.*, *23*, 147–154, doi:10.1007/s00367-003-0136-z.

Klein, S. (2006), Sediment porewater exchange and solute release during ebullition, *Mar. Chem.*, *102*, 60–71, doi:10.1016/j.marchem.2005.09.014.

L'Esperance, J. (2009), Simultaneous measurements of Young's modulus and Poisson's ratio of marine sediments with a simple uni-axial compression test, M.S. thesis, Dalhousie Univ., Halifax, Nova Scotia, Canada.

Martens, C., and J. Klump (1980), Biogeochemical cycling in an organic-rich coastal marine basin: 1. Methane sediment-water exchange processes, *Geochim. Cosmochim. Acta*, *44*, 471–490, doi:10.1016/0016-7037(80) 90045-9.

Matthews, J. E. (1982), Shear wave velocity measurements in marine sediments, *Geo Mar. Lett.*, *2*, 215–217, doi:10.1007/BF02462766.

McGinnis, D. F., J. Greinert, Y. Artemov, S. E. Beaubien, and A. Wüest (2006), Fate of rising methane bubbles in stratified waters: How much methane reaches the atmosphere?, *J. Geophys. Res.*, *111*, C09007, doi:10.1029/2005JC003183.

Menand, T., and S. Tait (2001), A phenomenological model for precursor volcanic eruptions, *Nature*, *411*, 678–680.

Menand, T., and S. Tait (2002), The propagation of a buoyant liquid-filled fissure from a source under constant pressure: An experimental approach, *J. Geophys. Res.*, *107*(B11), 2306, doi:10.1029/2001JB000589.

Orsi, T. H., and L. Anderson (1994), Bubble characteristics in gassy sediments, *Trans. Gulf Coast Assoc. Geol. Soc.*, *44*, 533–540.

Ostrovsky, I. (2003), Methane bubbles in Lake Kinneret: Quantification and temporal and spatial heterogeneity, *Limnol. Oceanogr.*, *48*, 1030–1036, doi:10.4319/lo.2003.48.3.1030.

Pilkey, W., D. Pilkey, and R. E. Peterson (2008), *Peterson's Stress Concentration Factors*, 3rd ed., John Wiley, Hoboken, N. J.

Reed, A., B. Boudreau, C. Algar, and Y. Furukawa (2005), Morphology of gas bubbles in mud: A microcomputed tomographic evaluation, paper presented at the International Conference on Underwater Acoustic Measurements: Technologies and Results, Found. for Res. and Technol., Inst. of Appl. and Comput. Math., Heraklion, Crete, Greece, 28 June to 1 July.

Rivalta, E., and T. Dahm (2006), Acceleration of buoyancy-driven fractures and magmatic dikes beneath the free surface, *Geophys. J. Int.*, *166*, 1424–1439, doi:10.1111/j.1365-246X.2006.02962.x.

Rivalta, E., M. Bottinger, and T. Dahm (2005), Buoyancy-driven fracture ascent: Experiments in layered gelatin, *J. Volcanol. Geotherm. Res.*, *144*, 273–285, doi:10.1016/j.jvolgeores.2004.11.030.

Sneddon, I. (1946), The distribution of stress in the neighborhood of a crack in an elastic solid, *Proc. R. Soc. London, Ser. A*, *187*, 229–260, doi:10.1098/rspa.1946.0077.

Takada, A. (1990), Experimental study on propagation of liquid-filled crack in gelatin shape and velocity in hydrostatic stress condition, *J. Geophys. Res.*, *95*, 8471–8481, doi:10.1029/JB095iB06p08471.

Timoshenko, S., and J. Goodier (1970), *Theory of Elasticity*, McGraw-Hill, New York.

van Kessel, T., and W. van Kesteren (2002), Gas production and transport in artificial sludge deposits, *Waste Manage.*, *22*, 19–28, doi:10.1016/S0956-053X(01)00021-6.

Walter, K., S. Zimov, J. Chanton, D. Verbyla, and L. Chapin III (2006), Methane bubbling from Siberian thaw lakes as a positive feedback to climate warming, *Nature*, *443*, 71–75, doi:10.1038/nature05040.

Walter, K., M. Edwards, G. Grosse, S. Zimov, and F. Chapin III (2007a), Thermokarst lakes as a source of atmospheric CH4 during the last deglaciation, *Science*, *318*, 633–636, doi:10.1126/science.1142924.

Walter, K., L. Smith, and F. Chapin III (2007b), Methane bubbling from northern lakes: Present and future contributions to the global methane budget, *Philos. Trans. R. Soc. Ser. A*, *365*, 1657–1676, doi:10.1098/rsta.2007.2036.

Weertman, J. (1971a), Theory of water-filled crevasses in glaciers applied to vertical magma transport beneath oceanic ridges, *J. Geophys. Res.*, *76*, 1171–1183, doi:10.1029/JB076i005p01171.

Weertman, J. (1971b), Velocity at which liquid-filled cracks move in the Earth's crust or in glaciers, *J. Geophys. Res.*, *76*, 8544–8553, doi:10.1029/JB076i035p08544.

Wheeler, S. J. (1988), A conceptual model for soils containing large gas bubbles, *Geotechnique*, *38*, 389–397, doi:10.1680/geot.1988.38.3.389.

Winterwerp, J., and W. van Kesteren (2004), *Introduction to the Physics of Cohesive Sediment in the Marine Environment*, Elsevier, Amsterdam.

Zhuang, Q., J. M. Melack, S. Zimov, K. M. Walter, C. L. Butenhoff, and M. A. K. Khalil (2009), Global methane emissions from wetlands, rice paddies, and lakes, *Eos Trans. AGU*, *90*(5), 37–38, doi:10.1029/2009EO050001.

C. K. Algar (corresponding author), The Ecosystems Center, Marine Biological Laboratory, 7 MBL St., Woods Hole, MA 02543, USA. (calgar@mbl.edu)

M. A. Barry and B. P. Boudreau, Department of Oceanography, Dalhousie University, Halifax, NS B3H4J1, Canada.